Accepted Manuscript

Volume 6
Number 12
28 March 2018
Pages 4883-5230

Journal of
Materials Chemistry A

Materials for energy and sustainability

rsc.li/materials-a

ISSN 2050-7488

ROYAL SOCIETY OF CHEMISTRY

COMMUNICATION
Zhenhai Wen et al.
An electrochemically neutralized energy-assisted low-cost acid-alkaline electrolyzer for energy-saving electrolysis hydrogen generation

This is an **Accepted Manuscript**, which has been through the Royal Society of Chemistry peer review process and has been accepted for publication.

Accepted Manuscripts are published online shortly after acceptance, before technical editing, formatting and proof reading. Using this free service, authors can make their results available to the community, in citable form, before we publish the edited article. We will replace this Accepted Manuscript with the edited and formatted Advance Article as soon as it is available.

You can find more information about Accepted Manuscripts in the Information for Authors.

Please note that technical editing may introduce minor changes to the text and/or graphics, which may alter content. The journal's standard Terms & Conditions and the Ethical guidelines still apply. In no event shall the Royal Society of Chemistry be held responsible for any errors or omissions in this Accepted Manuscript or any consequences arising from the use of any information it contains.

ROYAL SOCIETY OF CHEMISTRY

rsc.li/materials-a

Effect of Preconditioning on Cycling Performance

of Aqueous Zn-Ion Batteries

Neelam Sunariwal[1,2], Thanh Le[3], Xiaoran Yang[3], Trenton Gallagher[3], Jordi Cabana[1,2], Tim Vosburgh[3] and Sanja Tepavcevic[1*]

[1]Materials Science Division, Argonne National Laboratory, Lemont, IL 60439, United States
[2]Department of Chemistry, University of Illinois Chicago, Chicago, IL, 60608, United States
[3]Coulomb Technology, 8836 Sunfish Way, Suite 2207 Knoxville, TN, 37923, United States

*Email: sanja@anl.gov

Abstract

In this study, we provide valuable insights into the preconditioning effects on optimization of a zinc ion (Zn-MnO$_2$) battery with lower current rates. While other academic papers aim to provide fundamental insights and highly engineered approaches, this paper aims to provide a commercially relevant study that improves the performance of a full system that can be applied at scale. We demonstrate that fast C-rate preconditioning effectively improves the performance of Zn-MnO$_2$ full cells when used in synergy with an aqueous electrolyte with 1 vol% acetonitrile additive and optimized ZnSO$_4$ and MnSO$_4$ salt concentrations. Three cycles of preconditioning protocols using C/3 rate and 1C rate led to a remarkable specific discharge capacity of over 500 mAh g^{-1} for low loading cathodes of ~2 mg/cm^2 after 25 cycles at C/10 rate. Discharge capacity ~350 mAh g^{-1} and high coulombic efficiency of 99% can be maintained even after increasing electrode loadings to commercially relevant levels of ~6 mg/cm^2. These results demonstrate that preconditioning could activate internal restructuring of the electrolytic MnO$_2$ cathode during fast-rate cycling and can lead to the creation of more efficient pathways for both electrons and ions, improving the overall conductivity and Zn^{2+} transport. It highlights electrochemical preconditioning as a simple yet powerful strategy to achieve high specific discharge capacities in commercial aqueous zinc-ion batteries.

1. Introduction

Aqueous zinc-ion batteries (AZIBs) have emerged as new candidates for grid-scale and safe energy storage applications because of their intrinsic safety, low cost, and abundant materials.[1–3] Grid-storage, generally based on long-duration electricity storage (LDES) systems that are capable of discharging at their rated power for 10 hours or more, is increasingly recognized as essential for stabilizing modern grids.[4] Short-duration storage is well-suited to hourly balancing and routine day-to-day adjustments, whereas LDES addresses extended events and multi-day gaps driven by demand swings, planned or unplanned outages, transmission constraints, and seasonal variability. For multi-hour discharge durations typical of LDES (4-10 h), representative C-rates are C/4-C/10, with C/10 used for much of our evaluation to emulate long-duration duty.[5] This capability provides local, affordable, and resilient backup power for communities, critical facilities, and industry.[6,7]

Among available AZIB chemistries, manganese oxide (MnO_2) stands out as one of the best cathode materials because Mn is earth-abundant, non-toxic, and capable of exhibiting multiple valence states. Its theoretical capacity ranges from 308 to 616 mAh g^{-1}, depending on whether one or two electrons participate in the $Mn^{4+} > Mn^{2+}$ reduction process.[8] In addition, the Zn metal anode offers a high theoretical capacity (~820 mAh g^{-1}) and exhibits low activity toward hydrogen evolution in water-based electrolytes. The Zn-MnO_2 chemistry is known to be highly cost-effective, with prior techno-economic analyses reporting very low active-material costs of ≈US$5–10 kWh^{-1} for MnO_2/Zn cells.[6,7] In practice, it is difficult to translate these advantages into durable devices.[9,10] In particular, MnO_2 cathodes undergo phase transformations, structural collapse, and transition-metal dissolution, which deteriorate capacity and limit overall cycling performance.[6,9,11,12]

Historically, the development of AZIBs has aimed to suppress dissolution by stabilizing host frameworks through compositional tuning, protective coatings, surface doping, and electrolyte engineering.[10,11] Capacity fading due to Mn dissolution in Zn/MnO_2-based AZIB systems has traditionally been attributed to active-material loss. However, recent studies have demonstrated that dissolution chemistry could be harnessed as an operative component of the reaction pathway, exploiting reversible MnO_2 dissolution and redeposition as a standalone cathode mechanism in AZIBs.[13–16]

The dissolution-deposition route enables kinetic pathways that govern phase evolution in MnO_2-based electrodes. By controlling dissolution and redeposition, MnO_2/Mn^{2+} redox could be isolated from confounding side reactions to observe phase changes and can be tuned to enhance capacity rather than degrade it. This insight bridges the gap between additive-based strategies (e.g., Mn^{2+} seeding in the electrolyte) and a deliberate conversion mechanism that exploits the same equilibrium to achieve stable cycling. Finally, embracing dissolution–deposition opens a broader design space for aqueous batteries.[17,18]

Simple preconditioning steps could be a plausible strategy to reliably approach the two-electron $Mn^{4+} \leftrightarrow Mn^{2+}$ capacity.[19] Electrolyte wetting of the porous cathode, ideally by presoaking or brief

vacuum-assisted wetting, eliminates trapped air, reduces interfacial resistance, and promotes uniform MnO_2 nucleation during the first charge. Recently, an increasing number of studies have focused on high C-rate but low-capacity performance, which often deliver insufficient energy density requirements for practical zinc-ion batteries.[20] Wang et al, showed that an electrochemically induced layered MnO_2 cathode could provide 292.2 mAh/g, however, their results were at a current density of 1C.[21] Similarly, Liu et al reported that potassium pre-intercalated MnO2 nanosheet delivers a high capacity of 280 mAh/g at C/3 rate.[22] We believe that more systematic, fundamental research is necessary to develop an understanding of slow-rate cycling conditions that are more relevant to grid storage applications.

To explore the potential of achieving high capacities via a two-electron redox mechanism in AZIBs with electrolytic manganese dioxide (EMD) cathode chemistry, we conducted a systematic investigation into the influence of electrolyte salt concentration, cathode composition, and the effect of heat-temperature treatment and fast-charging preconditioning on electrochemical performance. We report that ball-milling of the EMD powder and slurry composition refinement in addition to electrolyte optimization with the manganese salt, improved initial capacity ramp-up. Established fast-to-slow cycling and short high-temperature preconditioning protocols gave the most significant sustainable capacity enhancement ~550 mAh g^{-1} for low loading cathodes (~2 mg/cm² EMD active material) without significantly compromising stability over 25 cycles at C/10 rate. We note that continuous high-T cycling gave the highest peak capacity (~600 mAh g^{-1}) but at the cost of rapid degradation. Discharge capacity ~350 mAh g^{-1} and high coulombic efficiency of 99% were maintained even after increasing electrode loadings to commercially relevant levels of ~6 mg/cm². Despite different approaches to promote wettability in high-loading cathodes, achieved discharge capacities were not further improved, underscoring the critical influence of electrolyte-electrode interfacial and bulk wetting and the need for new, hydrophilic binders, compatible with the aqueous electrolytes. Finally, the high-capacity results were reproduced by Coulomb Technology in their lab with the same cathode mass loading, demonstrating the reliability of the developed protocols.

2. Experimental Section

2.1 Synthesis of materials

Ultrafine electrolytic manganese dioxide (EMD, Borman) was prepared in a planetary mill (mechanochemical ballmill) using a zirconia jar and 5 mm ZrO_2 balls at 400 rpm, with a ball-to-powder mass ratio of 1:1.5 and isopropanol as the milling medium. The solution was milled for a total of 15 h in cycles of 30 min milling followed by 60 min rest to limit heat buildup and pressure in the sealed jar. After milling, the slurry was filtered to remove the media and dried at room temperature in a fume hood until the solvent had fully evaporated, yielding the ball-milled MnO_2 powder. The electrode slurry was prepared with a composition of 70 wt% ball-milled EMD, 20

wt% conductive carbon (C65), and 10 wt% polyvinylidene fluoride (PVDF) binder. N-methyl-2-pyrrolidone (NMP) served as the solvent, with an NMP-to-PVDF ratio of 92:8 wt%. The conductive carbon, active material, and binder–solvent solution were homogenized in a Thinky planetary mixer at 2000 rpm for 25 minutes. The slurry was cast onto stainless steel 304 (SS304) foil using a doctor blade. The coated electrodes were subsequently dried at 80 °C in an oven overnight and calendared. After drying, the low-loading cathode had a thickness of 27 μm, while the high-loading cathode was 55 μm thick.

2.2 Material Characterizations

X-ray powder diffraction of all the samples was performed using a laboratory PANalytical X'Pert PRO XRD instrument with Cu Kα radiation ($\lambda = 1.5418$ Å). Data were collected by scanning from 10° to 75°, 2θ, using a step size of 0.019°, at a rate of 2.6×10^{-5} min−1 2θ, using a custom air-free sample holder to avoid contamination from the air. Particle morphology was observed by Scanning electron microscopy (SEM) and energy dispersive X-ray (EDS) spectroscopy (JEOL JSM6610LV) equipped with EDS (Oxford Instruments) operating at 20 kV. During imaging, representative areas on the sample surface were selected, and a voltage of 5 kV was used.

2.3 Electrochemical Performance

Electrodes were punched from their respective foils at 1/2" diameter for Zn electrode discs, 3/8" for cathode electrodes, and 5/8" diameter for glass fiber separators. Zn sheets were polished with 400, 800, and 1000 grit sandpaper prior to punching, followed by cleaning with water, acetone, and isopropanol, and dried under low vacuum at room temperature prior to use.

Zn metal half-cells were built with MnO_2 as active material in the working electrode. The powders were either sieved or ball milled with conductive carbon (Super C65 from Imerys, typical Fe content of 2 ppm) in a 70:20:10 ratio with PVDF binder and slurry coated on the stainless-steel foil, and 80 mL of electrolyte was used. Zn metal foil was used as the counter and pseudo-reference, with Whatman GF/C borosilicate glass fiber sheets as separators, soaked in an electrolyte composed of 1M $ZnSO_4$ and 0.5M/1M $MnSO_4$ in Millipore water with 1 vol% acetonitrile (ACN). All cells were made in a 2032-coin cell for testing.

For coin cells, constant current (galvanostatic) cycling was performed at C/1, C/3, C/5, and C/10 rates. The currents were set using the theoretical capacity of the cathode active mass (EMD) by taking 2 electrons into consideration and dividing the specific capacity by 3 hours for C/3 and 10 hours for C/10 rate. All cells were rested for 3 hours before cycling with discharge as the first step. We conducted over the full usable voltage range determined by the electrolyte and electrode stability (0.9-1.0V), corresponding to ~100% EOD of the accessible capacity. Coin cell cycling was performed on a Biologic BCS-800 battery cycler at a room temperature (RT) of ~25°C, and a temperature-controlled chamber was used for cycling at 50°C. EIS was performed at an open circuit potential, and the perturbation from 1 Hz to 10 kHz is 10 mV. Coulomb Technology

reproduced our data using similar protocol of C/3 for 3 cycles followed by C/10 but without any rest period.

3. Results and Discussion

3.1 Optimization of aqueous Zn electrolyte

In this section, we examine the effect of $MnSO_4$ concentration on the $ZnSO_4$-based aqueous electrolyte on MnO_2 utilization and overall capacity retention. For that, the electrochemical performance of the Zn–MnO_2‖Zn coin cells were evaluated using an aqueous electrolyte composed of $ZnSO_4$ and $MnSO_4$. In our previous work, we demonstrated that incorporating a small fraction of ACN into $ZnSO_4$-based electrolytes induces an antisolvent effect, i.e., ACN molecules are excluded from the Zn^{2+} and SO_4^{2-} solvation shells in the bulk electrolyte and preferentially adsorb at the interface of electrode-electrolyte, thereby modifying the local solvation environment.[23] This interfacial restructuring results in more uniform Zn deposition, suppressed hydrogen evolution reaction (HER), and consequently, enhanced Zn plating/stripping efficiency. Specifically, low ACN concentrations (0.5–2 vol%) were found to minimize overpotentials and maximize the cumulative Coulombic efficiency (CE) over 100 cycles in both half-cell (Cu‖Zn) and full-cell (MnO_2‖Zn) configurations.[24] Based on these findings, a 1 vol% ACN additive was selected for the present study to optimize electrolyte performance while maintaining system stability.

Figure 1 shows galvanostatic charge-discharge (GCD) curves with a C/3 rate of Zn-MnO_2 full cells cycled in 1M $ZnSO_4$ with two different concentrations of $MnSO_4$ in the electrolyte, 1M and 0.5M. These two concentrations were selected based on prior studies showing that Mn^{2+} additives stabilize the MnO_2 cathode by compensating dissolution losses, but excessive Mn^{2+} can suppress MnO_2 utilization and alter the dissolution-redeposition equilibrium. Thus, 0.5 M and 1 M $MnSO_4$ represent two regimes of interest: a lower bound that still provides a Mn reservoir, and a higher bound commonly used in literature for dissolution compensation. In a 1M $ZnSO_4$ and 1M $MnSO_4$ electrolyte, a specific capacity of ~250 mAh/g was delivered after 25 cycles, whereas in 1M $ZnSO_4$ and 0.5M $MnSO_4$, the specific capacity progressively reached up to ~340 mAh/g after 25 cycles. This observation of increasing capacity in the 0.5 M $MnSO_4$ electrolyte aligns with prior reports showing a Mn^{2+} effect is concentration-dependent i.e., at moderate Mn^{2+} levels, Mn^{2+} is electro-oxidized and redeposited on the cathode to compensate for Mn dissolution, but at higher concentrations, undesirable phase transitions consume the Mn^{2+} reservoir and degrade performance.[25,26] Thus, it is crucial to choose an optimum $MnSO_4$ concentration where the Mn reservoir is sufficient to stabilize the cathode without significantly blocking ion transport or altering interfacial reactions.[27–29]

Therefore, we selected 0.5 M $MnSO_4$ for all subsequent experiments and focused on improving MnO_2 utilization through cathode microstructure and preconditioning rather than further electrolyte Mn^{2+} enrichment.
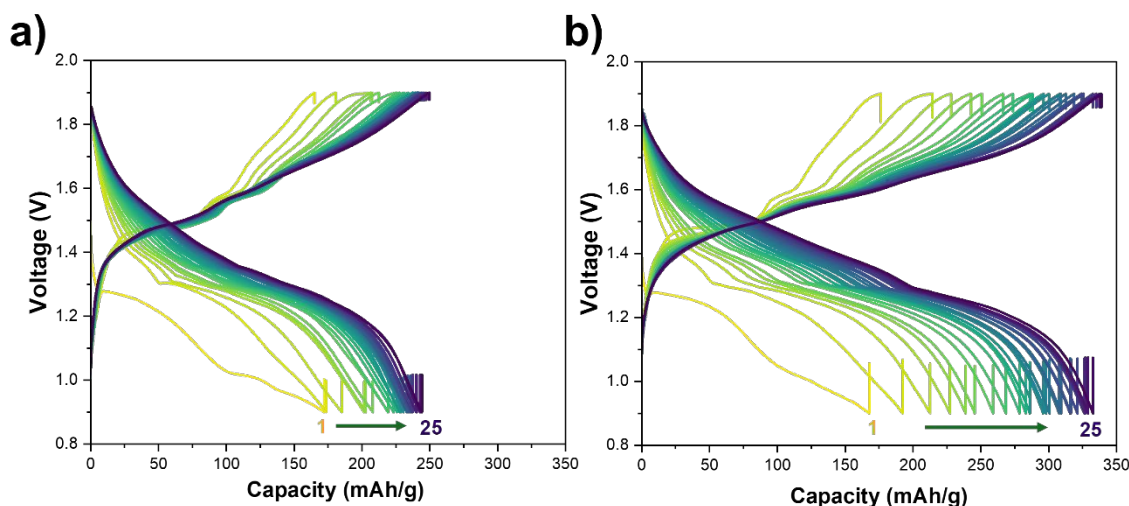

Figure 1: **Optimization of aqueous Zn electrolyte**. Effect of electrolyte salt concentration on cycling performance: 1M $ZnSO_4$ with 1 vol% ACN additive and a) 1M $MnSO_4$, b) 0.5M $MnSO_4$. Comparison of capacity retention at C/3 rate for the initial 25 cycles on stainless steel current collector at room temperature.
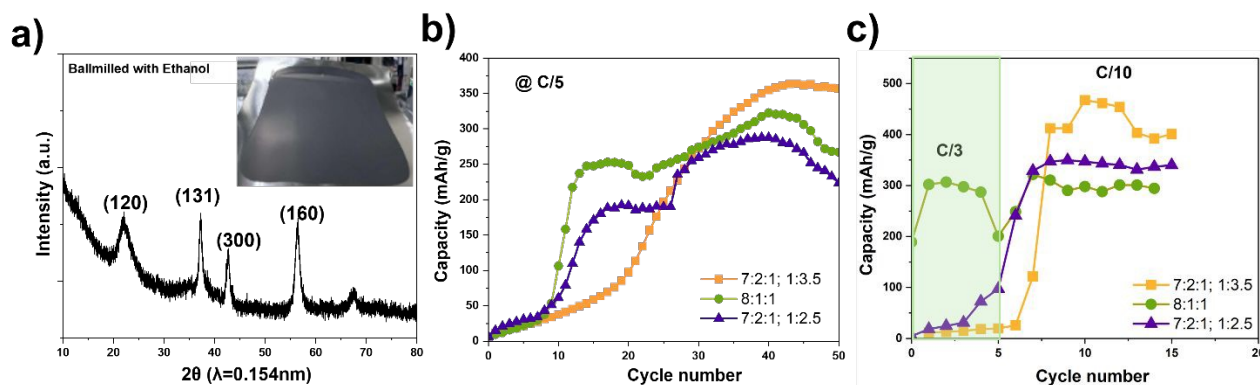
3.2 Optimization of MnO_2 Cathode Composition

Figure 2a shows the XRD pattern of ball-milled electrolytic MnO_2 powder (EMD) with ethanol. The structure of EMD is dominated by the γ-phase with 1x1 and 1x2 tunnels, and the relative fractions of these could control the favorable pathways for Zn^{2+}/H^+ insertion and diffusion, which governs the electrochemical performance of EMD.[8,30] We performed mechanochemical ball milling of MnO_2 powder to ensure uniform particle size and increased structural disorder, which enhances ion transport and increases the number of electrochemically active sites throughout the material. The SEM images of ballmilled EMD are shown in Figure S1. Mechanochemical ball milling can also introduce oxygen vacancies for MnO_2, thus increasing the active sites for redox reactions and significantly improving the electrochemical performance of the materials.[31–33]

The active cathode materials are often powders or pastes that lack structural integrity on their own. The metal foil provides robust, flexible mechanical support, which is critical for high-speed, large-scale manufacturing processes like roll-to-roll coating. Furthermore, using a thin metal foil (modern batteries use foils as thin as 8-10 micrometers) helps to minimize the weight of non-active

components in the battery, thereby maximizing the overall energy density. We employed SS304 foil as the current collector of choice due to its low cost, electrochemical stability in mild aqueous electrolytes, and easy slurry coating for manufacturing due to its good adhesion.[3]

Here, we aim to optimize the ratio of MnO_2, carbon, and PVDF, as well as slurry solids content (solute-to-solvent ratio), to investigate its influence on electrode microstructure and thus achievable capacity at moderate rates. The composition ratios are given as EMD:Carbon:PVDF. For this, we systematically prepared three slurry coatings on stainless steel (SS304), namely 7:2:1 composition with 1:3.5 solute to solvent ratio (coating-1), 7:2:1 composition (coating-2), and 8:1:1 composition (coating-3) with 1:2.5 solute to solvent ratio. Figure 2b shows cell cycling data with all three coatings at a C/5 rate. From the cycling plot, we observed that all three coatings start at the same place and go up in capacity as the cycle number increases. After 10 cycles, coating-2 and coating-3 deliver higher capacity compared to coating-1, 180 mAh/g, 250 mAh/g, and ~40 mAh/g, respectively. Although coating-1 takes longer to go up in capacity than the other two coatings, it still delivers not only sustainable capacity after 50 cycles but also reaches higher levels compared to the others. This observation suggests that slower activation, but ultimately higher capacity of coating-1 could be due to its lower solids content (1:3.5 solute:solvent) that leads to a more porous, tortuous structure that initially suffers from poor wetting and ion transport. As cycling proceeds, electrolyte gradually infiltrates deeper into the cathode, unlocking additional active material and causing the capacity to rise. In contrast, the denser coatings (coating-2 and coating-3) appear to be more readily wetted and initially accessible, giving higher early-cycle capacity but saturating at lower ultimate values.

Figure 2: **Optimization of MnO_2 Cathode Microstructure and Composition** a) Powder X-ray diffraction pattern of ball-milled EMD MnO_2 with ethanol and coated MnO_2 cathode on stainless steel foil (inset); b) Cycling comparison of different slurry ratios and c) at fast to slow rates for three compositions.

Furthermore, we evaluated the specific capacity of the three coatings by cycling them at two different C-rates, as shown in Figure 2c. All samples were initially cycled for five cycles at a C/3 rate, followed by a C/10 rate for 10 cycles in coating-1, coating-2, and coating-3. Initially cycling with C/3 rate, coatings-1 and coating-2 exhibited comparable initial discharge capacity, while

coating-3 already achieved a specific capacity of approximately ~300 mAh g⁻¹. After switching to the C/10 rate, the capacity of coating-3 showed only modest improvement, indicating limited rate dependence, while coating-2 reached a specific capacity of ~340 mAh g⁻¹ at C/10. Notably, coating-1 demonstrated the highest achievable capacity ~460 mAh g⁻¹ at C/10, highlighting its optimized composition and the critical role of solute-to-solvent ratio in determining electrochemical behavior. The strong rate dependence of coating-1 (460 mAh/g at C/10) compared to the limited gains in coating-3 implies that, in the optimized composition, high capacities are unlocked only once ionic transport limitations are mitigated. Since coating-1 combines the highest ultimate capacity with realistic coating properties, we adopt it for all subsequent preconditioning studies.

These cycling results suggested that Zn-MnO₂ batteries might benefit from initial pre-conditioning to achieve high specific capacity. To better understand the effect of initial cycling conditions on the overall specific capacity of the cell, we focused on two preconditioning strategies: 1) initial cycling at high temperature, 50°C followed by RT cycling, at constant C-rate, and 2) starting with a fast-charging protocol followed by a slow C-rate at RT.
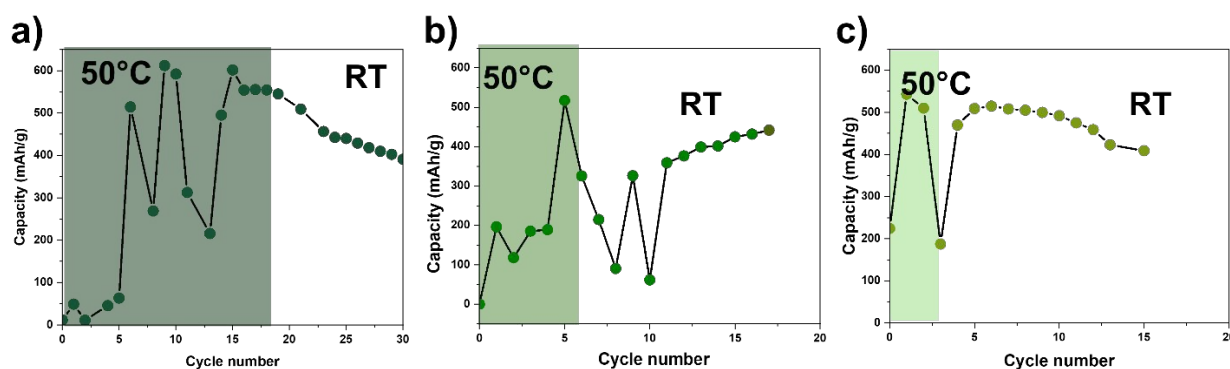

Figure 3: **High Temperature Preconditioning of Zn- MnO₂ Full Cells.** Capacity retention at C/10 rate with high temperature preconditioning at 50°C for a) 20 cycles, b) 6 cycles, and c) 3 cycles, followed by 10 cycles at room temperature.

3.3 Effect of Preconditioning on Cycling Performance: High Temperature

We hypothesize that elevated temperature enhances Zn²⁺ transport and electrode wetting, thereby accelerating activation and enabling capacities closer to the theoretical limit. To probe the electrochemical kinetics of the coated EMD electrode (coating-1) with temperature, three-coin cells replicates were initially run for a few cycles at 50°C, followed by room temperature cycling. Figure 3 compares the effect of 20, 6, and 3 cycles at 50°C. As can be seen from these graphs, cycling at high temperatures might be associated with an increase the electrochemical kinetics in the system and assisted in achieving a higher specific capacity of ~600mAh/g. However, after switching these cells to cycle at RT, the capacity undergoes fluctuations. This observation indicates that although high temperature cycling enabled capacities exceeding 500-600 mAh/g, these gains

were not sustainable. The rapid capacity fading suggests that accelerated parasitic reactions, such as electrolyte decomposition, corrosion, or irreversible structural transformations, could offset the benefits of improved kinetics. This result highlights a key limitation of using thermal preconditioning, which is beneficial in revealing the intrinsic capacity of the system but is not a practical route to durable performance under mild conditions. These observations motivated us to seek an alternative activation pathway that could improve wetting and kinetics without incurring the stability penalties associated with elevated temperature.

3.4 Effect of Preconditioning on Cycling Performance: Fast-rate

To develop an alternative activation strategy that enhances both Zn^{2+} transport and MnO_2 utilization without relying on elevated temperature, we investigated fast-rate preconditioning at room temperature. Our goal was to determine whether brief high-current cycling could replicate the beneficial effects of high-temperature activation while avoiding accelerated degradation. We compared two fast rate preconditioning protocols: (a) three initial cycles at 1C and (b) three initial cycles at C/3, followed in both cases by long-term cycling at C/10 (Figures 4a and 4b). During 1C preconditioning, the initial discharge capacity was approximately 100 mAh g^{-1}, which increased to ~500 mAh g^{-1} upon transitioning to the slower C/10 rate. Similarly, for C/3 preconditioning, the initial discharge capacity was ~200 mAh g^{-1}, increasing to ~550 mAh g^{-1} at C/10. Notably, fast-rate preconditioning at room temperature achieves capacities approaching those observed under high-temperature cycling (~500-600 mAh g^{-1}). These results demonstrate two key points: First, similar to high-temperature preconditioning, fast-rate cycling can unlock capacities approaching the theoretical limit of MnO_2 (~616 mAh g−1), implying that the intrinsic Zn^{2+} storage capability of the EMD cathode is high but initially hindered by kinetic and/or transport limitations. Second, the superior retention for C/3 relative to 1C suggests that overly aggressive activation may introduce additional degradation pathways (e.g., excessive dissolution or particle fracture) that partially offset the benefits of improved kinetics.
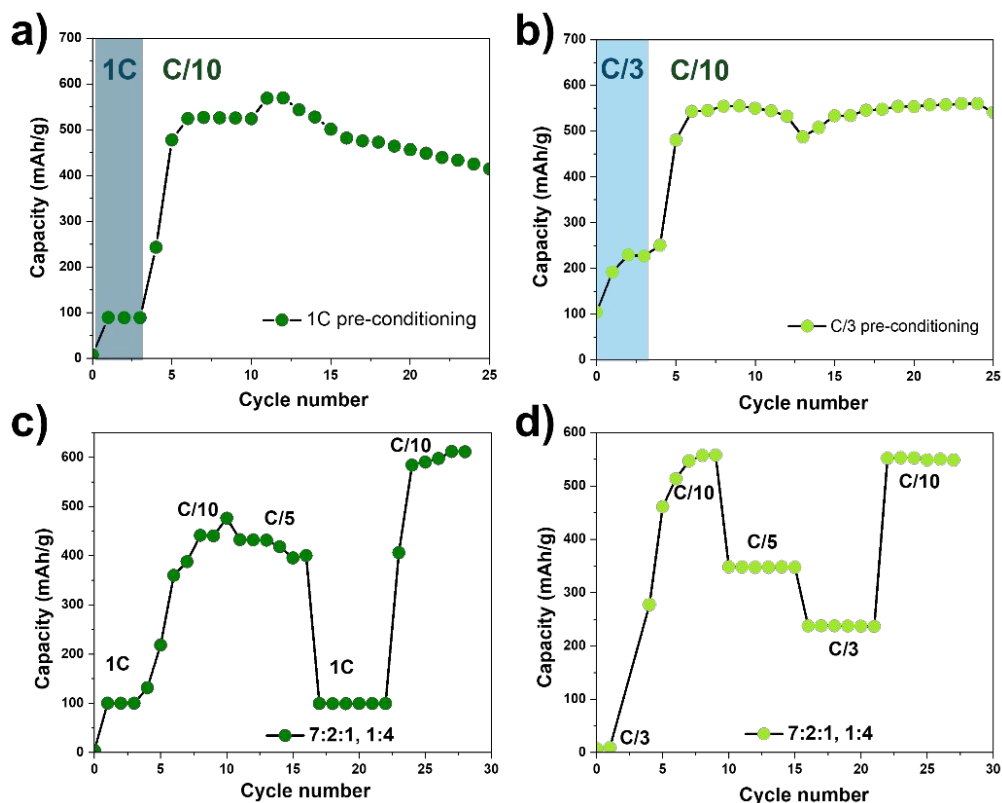
Figure 4: **Fast Rate Preconditioning of Zn- MnO$_2$ Full Cells** a) with 1C rate for three cycles and b) with C/3 rate for three cycles. c) and d) are rate tests at room temperature (RT), starting with 1C and C/3, respectively.

To probe the underlying kinetic changes induced by fast-rate preconditioning, we performed electrochemical impedance spectroscopy (EIS) before cycling and after three preconditioning cycles at 1C and C/3 (Figure S2). The collected and fitted impedance spectra shows a high frequency intercept related to electronic resistance (R$_e$), a mid-frequency semicircle associated with a charge transfer resistance (R$_{ct}$), followed by a Warburg impedance (W$_d$) which is a slope at 45° at low frequency region characteristic of ion diffusion behavior.[34,35] Spectral fits for both plots revealed improved electronic transport after preconditioning treatment, likely due to more uniform distribution and better physical contact between the active material particles and conductive additives (Re in table of Figure S2). We discovered that preconditioning process also led to a significant decrease in charge-transfer resistance (R$_{ct}$) and Warburg impedance (W$_d$) at both 1C and C/3 rates, indicating improved interfacial kinetics and significantly enhanced ion diffusion within the electrode. We hypothesize that the fast rate preconditioning strategy is acting as an activation step for the MnO$_2$ cathode and improves electrolyte infiltration into porous agglomerates, lowering tortuosity and ionic resistance. This in turn, accelerates access to redox-active Mn sites and improves interfacial contact. This is consistent with the reduced charge-transfer resistance (smaller R$_{ct}$ semicircle) observed by EIS. Collectively, improved

wetting/transport potentially removes kinetic bottlenecks and underpins the capacity gains observed during subsequent C/10 cycling.

To assess whether conventional rate testing is sufficient to induce these beneficial transformations, we compared the standard slow-to-fast protocol (starting at C/10 and increasing) with a modified protocol that begins with fast-rate preconditioning (Figures S3 and 4c–d). Using the conventional rate capability protocol (Figure S3), the average discharge capacity at each C-rate changes only moderately as the rate increases (from C/10 to C/3), indicating relatively weak rate dependence. However, the capacity within some rate steps (especially C/10 and C/15) shows noticeable fluctuations, suggesting that this protocol does not effectively activate the electrode or stabilize its early-cycle behavior. We modified a new rate protocol by starting with a faster C-rate for the initial three cycles before implementing the conventional slow-to-fast rate sequence. To do that, we cycled the initial three cycles with 1C or C/3 rates, then followed with C/10, C/5, 1C or C/3, and back to C/10 rates, each for five cycles, as shown in Figure 4c &d. These rate-capabilities test results again indicate that C/3 rate preconditioning is an efficient way to deliver high and stable specific capacities. Importantly, capacities recovery was observed when returning to C/10 rate. While we ascribe these improvements largely to enhanced wetting and limited dissolution/redeposition, we cannot entirely rule out contributions from microcracking, particle rearrangements, or changes in solid-electrolyte interphase composition. Detailed in-situ structural and chemical characterization would be required to disentangle these effects.

To probe whether the activation observed under fast-rate preconditioning is driven by improved wetting, we introduced a cathode-only heat-treatment to promote electrolyte infiltration without applying current. The coated EMD cathode was exposed to 50 °C for 5 min in the presence of electrolyte to enhance penetration into the porous network. The cell was then assembled and subjected to our standard C/3 preconditioning followed by C/10 cycling (Fig. 5). Capacity increased from an initial ~120 mAh g^{-1} to ~500 mAh g^{-1} at C/10, with ~95% retention over 20 cycles. EIS revealed a notable decrease in charge-transfer resistance (R_{ct}) and Warburg diffusion impedance (W_d), despite a modest rise in series (electronic) resistance (R_e), indicating improved ionic accessibility and diffusion within the electrode. These results support that enhanced wettability is a key contributor to early activation, while fast-rate preconditioning provides complementary overpotential-driven interfacial reorganization that together yield the observed capacity gains.
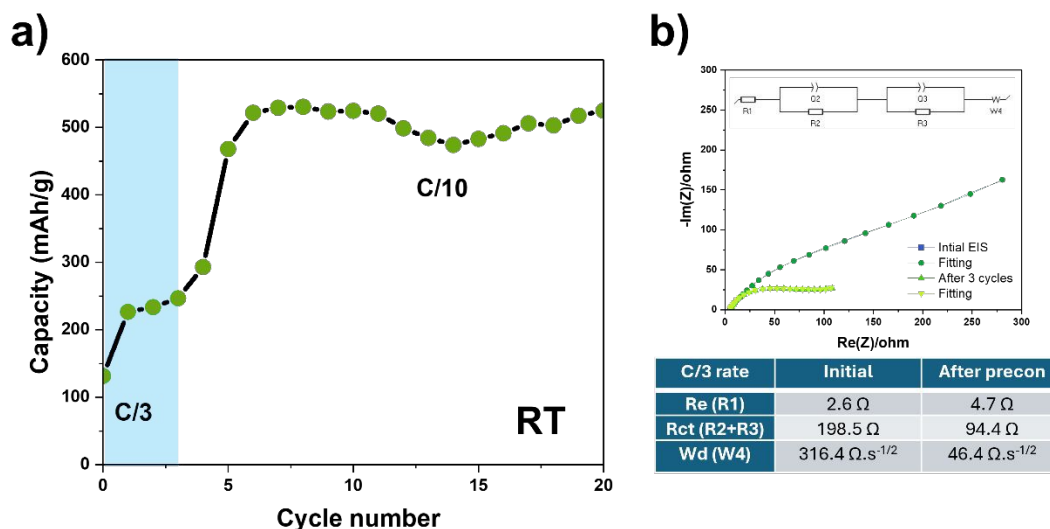
Figure 5: **Heat-treatment of EMD Cathode.** Heat-treated EMD cathode at 50°C for 5 minutes with electrolyte. a) Capacity retention of fast rate C/3 preconditioned at, followed by cycling at C/10 at room temperature and b) respective EIS before and after C/3 preconditioning.

Together, the results from fast-rate preconditioning and cathode-only heat treatment provide convergent evidence that early activation in Zn-MnO$_2$ cells is governed by electrolyte infiltration and ion transport within the EMD cathode. C/3 preconditioning imposes repeated overpotentials and sustained ion flux, enhancing wetting, lowering diffusion barriers, and accelerating structural adjustment of MnO$_2$. By thermally treating the cathode in the presence of electrolyte without applying current, we isolate the effect of wetting from electrochemical restructuring. The similar capacity gains and decreases in R$_{ct}$ and W$_d$ after subsequent C/3 preconditioning indicate that current-driven changes improving interfacial. The high capacity in heat-treated cathode cell was observed after fast-rate preconditioning, suggesting that purely physical wetting improvements are necessary but not sufficient; electrochemical driving forces are still required for complete activation of internal Mn sites. Since both fast-rate preconditioning and heat-treatment proved effective at low loadings by improving wetting and transport, we next tested whether these strategies can similarly activate thick, practical industry-relevant electrodes where bulk diffusion limitations are more severe.

3.5 Effect of EMD cathode loading with fast-rate preconditioning

To assess the relevance of our activation strategy for practical devices, we examined whether fast-rate preconditioning remains effective as cathode mass loading increases toward commercially relevant values (~6 mg/cm^2). This cycling was performed at Coulomb Technology laboratories to ensure compliance with commercial benchmarks. As shown in Figure 6a, the cell with the lowest active mass exhibited a sharp increase in charge capacity to ~600 mAh/g, with a corresponding discharge capacity of ~550 mAh/g, right after three C/3 preconditioning cycles. When the cathode

mass loading was slightly increased to 2.2 mg/cm² (Figure S5 a), the discharge capacity remained comparable at ~500 mAh/g, indicating good reproducibility. In contrast, when the mass loadings were increased threefold (Figures 6b and Figure S5 b), the specific capacity increase after the initial preconditioning step was gradual. Roughly after 15 cycles, both high-loading cathodes stabilized at ~350 mAh g⁻¹ and coulombic efficiency across all cells with higher loadings remains ~99%, confirming excellent reversibility and stable cycling behavior. Figure S4 shows an excellent capacity retention for 60 cycles for high-loading (6.2 mg/cm²) EMD cathodes, indicating their long-term performance. This suggests that as loading increases, the dominant limitation shifts from intrinsic redox capacity to mass transport within the thicker electrode. Even after preconditioning, electrolyte penetration and Zn^{2+} diffusion appear incomplete throughout the full thickness, leaving a fraction of active material underutilized. The fact that CE remains ~99% at high loading indicates that the reactions within the wetted volume are highly reversible; the bottleneck is accessing the deeper regions of the electrode. This observation is fully consistent with the wetting and diffusion limitations identified in the low-loading studies and underscores the need to engineer binder chemistry and pore architecture specifically for aqueous systems. Binders like PVDF that we are using here were originally designed for non-aqueous Li-ion battery systems and are inherently hydrophobic (water-repelling) due to their high fluorine content. Aqueous electrolytes have a high surface tension and struggle to permeate and effectively wet the porous cathode electrode structure and the surface of the active materials, and this poor wetting is a common and significant problem that needs to be resolved by the development of new hydrophilic binders compatible with aqueous electrolytes.[36]
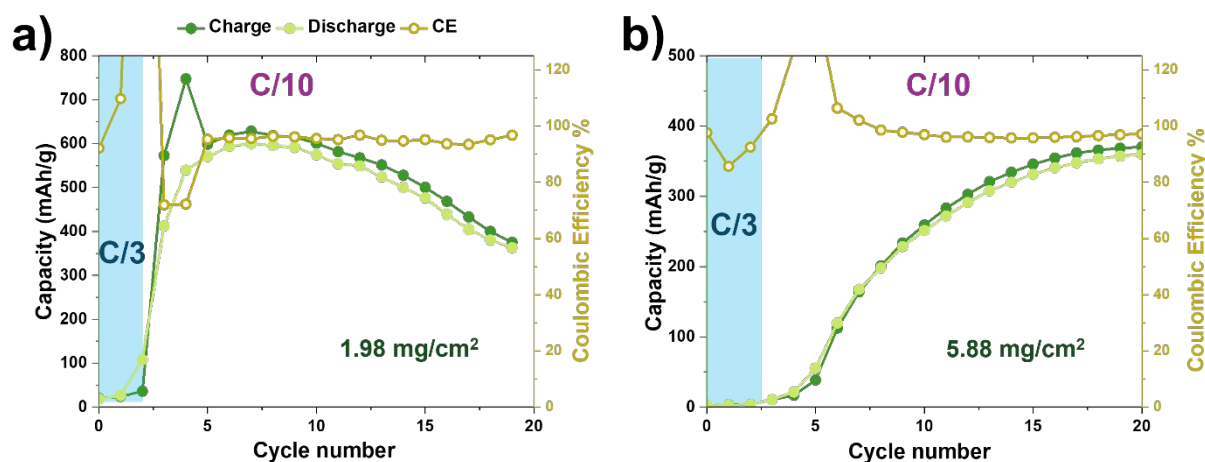

Figure 6: **Effect of EMD Cathode Loading on Achieved Capacity** C/3 fast rate preconditioning for coin-cells with a) 1.98mg/cm² and b) 5.88mg/ cm² cathode mass loadings.

Following our cycling results, we measured powder XRD for our cycled cathodes at different states of charge. As we discussed above, the initial state of the EMD cathode is the γ-phase of MnO_2. To establish clearer correlations between structural changes and capacity improvements after fast-rate preconditioning, we performed XRD experiments in both end of charge (EOC) and end of discharged (EOD) states, immediately after 3 preconditioning cycles at a C/3 rate (cycle 3) and after the first subsequent cycle at a C/10 rate (cycle 4) (Figure 7a). In the EOC state, the peaks of the γ-phase decrease, and we observed a shift of the peaks around 21°, 37°, and 42° towards a lower 2θ value, which we ascribed to the formation of a $ZnMn_2O_4$ type spinel phase.[37] While these peaks remained at the same 2θ values at the end of discharge, new peaks arose at low 2θ around 12° and around 25° appeared, which were ascribed to a layered δ-phase.[38] These results show that the γ-MnO_2 transforms into layered δ-MnO_2 in the discharged state, consistent with Zn–insertion pathways, along with the initial emergence of spinel-like features at early stages.
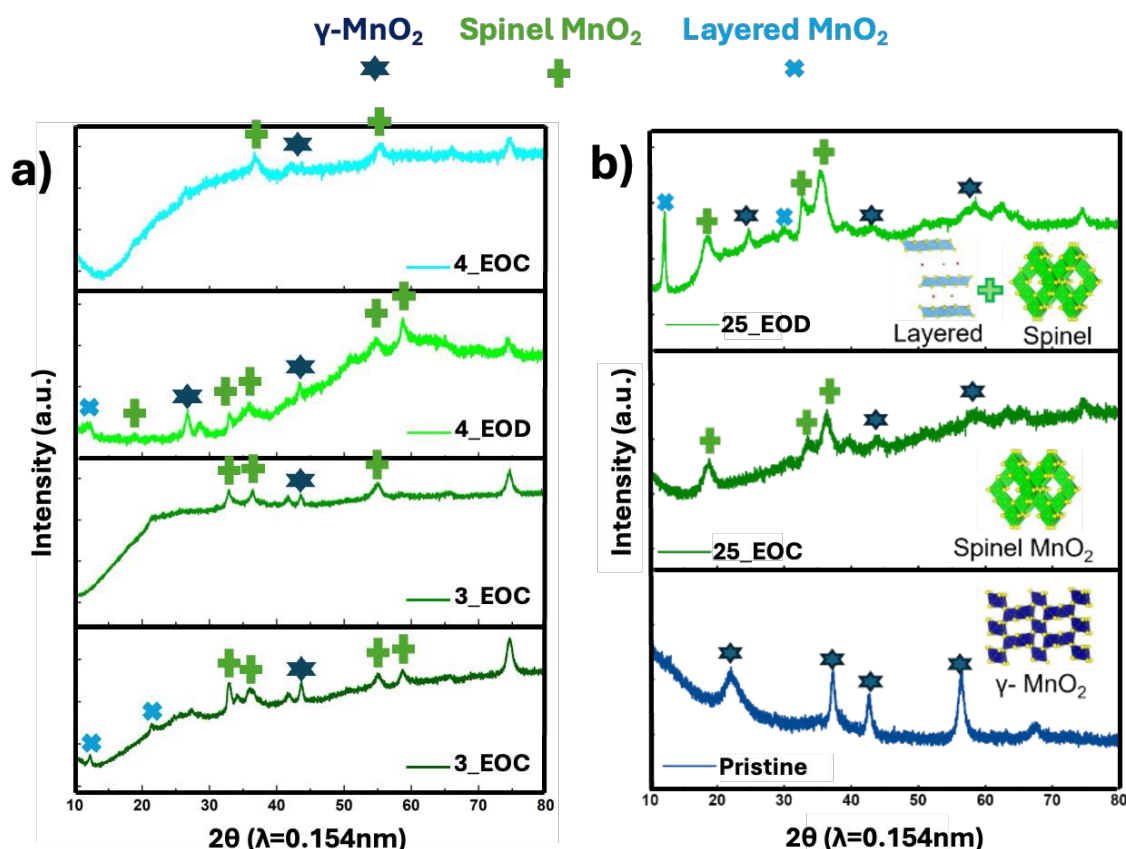
Figure 7: **Cycling Induced Phase Transformations of Electrolytic EMD:** Powder X-ray diffraction pattern of ball-milled EMD for pristine, right after preconditioning step (cycles 3 and 4) and after prolong cycling at 25 cycles for end of charge (EOC) and end of discharge (EOD) for low loading cathode (1.98mg).

When Zn intercalation proceeds to later stages (e.g., after 25 cycles), the δ- MnO_2 phase that is responsible for the high capacity remains present, while the spinel-related reflections become increasingly intense (Figure 7b). This suggests progressive development of spinel-like domains during cycling, superimposed on a still-active δ- MnO_2 framework. Regardless of cathode loading, we still see similar phases in the EOD sample for high loading cathode as well (Shown in Figure S6). While definitive assignment of all intermediates requires additional in situ probes, in-depth resolved information, post-mortem studies, including direct quantification of Mn dissolution and are planned for future work in order to evaluate detailed mechanistic understanding; the current available data supports the operational mechanism. A summary table of all experiments that includes details on current collector (foil), preconditioning cycling, main cycling, cathode loading, discharge capacity and interpretation is shown in Table S1. Our results show that we could achieve the highest specific capacity by using fast-rate preconditioning for different current collectors, indicating solely kinetics/wetting effects.

Across electrolyte formulation, microstructure tuning, fast-rate preconditioning, and heat-assisted infiltration, the strategies that most effectively increase Zn^{2+} access to the MnO_2 framework deliver the largest capacity gains, particularly at practical mass loadings where bulk intercalation, not surface reactions governs performance. Early-cycle activation, whether electrochemical (fast-rate) or thermal (infiltration), promotes formation of layered δ-MnO_2/buserite-like domains and related phases that better accommodate reversible Zn^{2+} storage. By improving Zn^{2+} transport and guiding the initial phase transformation while mitigating loss of structural water and degradation of layered, hydrated phases, these approaches enhance MnO_2 utilization and enable the retention of high specific capacity even as mass loading increases.[39] Achieving this combination of high capacity and high mass loading is critical for advancing large-scale grid-relevant energy storage applications, where practical energy density, rather than gravimetric capacity alone defines technological value.[40] Future studies should explore more preconditioning effects such as pulse-mode current application and steps performed separately from the electrolyte environment. These strategies may improve ion transport pathways, mitigate early-stage polarization, and facilitate faster activation of the electrode, thereby enabling higher accessible capacity further advance Zn-ion aqueous battery performance.

4. Conclusion

In the summary, we demonstrated the critical role of salt concentration and cathode composition in governing the performance and durability of Zn-MnO_2 batteries using aqueous electrolyte containing low concentrations of ACN (1 vol%) as antisolvent. By combining electrolyte engineering with tailored preconditioning, we show that high discharge capacities approaching the theoretical value of MnO_2 (~616 mAh g^{-1}) are attainable. Preconditioning using either cycling at high temperature or fast rate cycling enabled substantial capacity activation. However, extended high temperature cycling leads to parasitic reactions, compromising durability, whereas fast-rate

preconditioning for a few cycles at room temperature provided a more practical route to improved performance. We developed fast-to-slow cycling and short high-temperature preconditioning protocols that gave the most significant sustainable capacity enhancement of ~550 mAh/g for low ~2 mg/cm^2 EMD active material loading without significantly compromising stability over 25 cycles at C/10 rate. Discharge capacity ~350 mAh g^{-1} and high coulombic efficiency of 99% were maintained even after increasing electrode loadings to commercially relevant levels of ~6 mg/cm^2. Despite different approaches to promote wettability in high-loading EMD cathodes, the achieved discharge capacities were not further improved, underscoring the critical challenge of electrolyte-electrode interfacial and bulk wetting and the need for new, hydrophilic binders compatible with the aqueous electrolytes. Furthermore, future work should further explore the mechanisms of the structural changes in manganese dioxide cathodes during fast rate preconditioning and develop strategies for preserving high specific capacities at practically relevant, slow discharge rates.

Author contributions

Neelam Sunariwal: conceptualization, methodology, investigation, validation, resources, writing-original draft, and visualization. Thanh Le: methodology, validation, resources, writing-review and editing. Xiaoran Yang: methodology, writing-review and editing. Trenton Gallagher: investigation and writing-review and editing. Jordi Cabana: writing-review and editing. Tim Vosburgh: project administration, and funding acquisition. Sanja Tepavcevic: conceptualization, writing, review and editing, supervision, project administration, and funding acquisition.

Conflicts of interest

There are no conflicts to declare.

Acknowledgements

References:

1 E. D. Spoerke, H. Passell, G. Cowles, T. N. Lambert, G. G. Yadav, J. Huang, S. Banerjee and B. Chalamala, *MRS Energy & Sustainability*, 2022, **9**, 13–18.

2 J. Kumankuma-Sarpong, W. Guo and Y. Fu, *Advanced Energy and Sustainability Research*, 2022, **3**, 2100220.

3 H. Li, L. Li, W. Liu, S. Jia, S. Yue, Y. Yang, C. Wang, C. Tan and D. Zhang, *The Chemical Record*, 2025, **25**, e202400217.

4 P. Albertus, J. S. Manser and S. Litzelman, *Joule*, 2020, **4**, 21–32.

5 P. Albertus, J. S. Manser and S. Litzelman, *Joule*, 2020, **4**, 21–32.

6 C. Zhong, B. Liu, J. Ding, X. Liu, Y. Zhong, Y. Li, C. Sun, X. Han, Y. Deng, N. Zhao and W. Hu, *Nat Energy*, 2020, **5**, 440–449.

7 Findings from Storage Innovations 2030: Zinc Batteries, https://www.energy.gov/sites/default/files/2023-09/5_Technology%20Strategy%20Assessment%20-%20%235%20Zinc%20Batteries_508.pdf, (accessed October 31, 2025).

8 M. Musil, B. Choi and A. Tsutsumi, *J. Electrochem. Soc.*, 2015, **162**, A2058.

9 J. Yi, P. Liang, X. Liu, K. Wu, Y. Liu, Y. Wang, Y. Xia and J. Zhang, *Energy Environ. Sci.*, 2018, **11**, 3075–3095.

10 B. Zhang, P. Dong, S. Yuan, Y. Zhang, Y. Zhang and Y. Wang, *Chem Bio Eng.*, 2024, **1**, 113–132.

11 N. Zhang, F. Cheng, J. Liu, L. Wang, X. Long, X. Liu, F. Li and J. Chen, *Nat Commun*, 2017, **8**, 405.

12 H. Yao, H. Yu, Y. Zheng, N. W. Li, S. Li, D. Luan, X. W. (David) Lou and L. Yu, *Angewandte Chemie International Edition*, 2023, **62**, e202315257.

13 N. Becknell, P. P. Lopes, T. Hatsukade, X. Zhou, Y. Liu, B. Fisher, D. Y. Chung, M. G. Kanatzidis, N. M. Markovic, S. Tepavcevic and V. R. Stamenkovic, *Advanced Functional Materials*, 2021, **31**, 2102135.

14 T.-H. Wu, Y.-Q. Lin, Z. D. Althouse and N. Liu, *ACS Appl. Energy Mater.*, 2021, **4**, 12267–12274.

15 N. Li, S. Sallis, J. K. Papp, J. Wei, B. D. McCloskey, W. Yang and W. Tong, *ACS Energy Lett.*, 2019, **4**, 2836–2842.

16 H. Wang, L. Hu, H. Xu and J. Liu, *ACS Nano*, 2025, **19**, 22645–22680.

17 L. Liu, Y.-C. Wu, L. Huang, K. Liu, B. Duployer, P. Rozier, P.-L. Taberna and P. Simon, *Advanced Energy Materials*, 2021, **11**, 2101287.

18 C. Xian, R. He, Q. Chen, Q. Li, Y. Ma, S. Bao, W. Sun, H. Chen and M. Xu, *Chemical Engineering Journal*, 2025, **512**, 162576.

19 H. Wang, T. Wang, G. Stevenson, M. Chamoun and R. W. Lindström, *Energy Storage Materials*, 2023, **63**, 103008.

20 C. Li, S. Jin, L. A. Archer and L. F. Nazar, *Joule*, 2022, **6**, 1733–1738.

21 L. Wang, F. Wang, S. Huang and J. Chen, *Chemical Engineering Journal*, 2025, **515**, 163387.

22 L. Liu, Y.-C. Wu, L. Huang, K. Liu, B. Duployer, P. Rozier, P.-L. Taberna and P. Simon, *Advanced Energy Materials*, 2021, **11**, 2101287.

23 S. Ilic, M. J. Counihan, S. N. Lavan, Y. Yang, Y. Jiang, D. Dhakal, J. Mars, E. N. Antonio, L. Kitsu Iglesias, T. T. Fister, Y. Zhang, E. J. Maginn, M. F. Toney, R. F. Klie, J. G. Connell and S. Tepavcevic, *ACS Energy Lett.*, 2024, **9**, 201–208.

24   M. J. Counihan, L. Roberts, S. Ilic, Y. Yang, C. Ely, R. F. Klie, M. F. Toney and S. Tepavcevic, *J. Mater. Chem. A*, 2025, **13**, 17730–17739.

25   S. Cui, D. Zhang and Y. Gan, *Journal of Power Sources*, 2023, **579**, 233293.

26   C. Qiu, X. Zhu, L. Xue, M. Ni, Y. Zhao, B. Liu and H. Xia, *Electrochimica Acta*, 2020, **351**, 136445.

27   F. Wubatu Fenta and R. Bouchal, *Journal of Materials Chemistry A*, 2024, **12**, 25035–25046.

28   H. Yang, W. Zhou, D. Chen, J. Liu, Z. Yuan, M. Lu, L. Shen, V. Shulga, W. Han and D. Chao, *Energy Environ. Sci.*, 2022, **15**, 1106–1118.

29   R. Jian, A. Mashhadian, C. Wang, T. Hwang, Y. Hao, K. Cho and G. Xiong, *ACS Appl. Energy Mater.*, 2025, **8**, 12460–12479.

30   T. N. T. Tran, S. Jin, M. Cuisinier, B. D. Adams and D. G. Ivey, *Sci Rep*, 2021, **11**, 20777.

31   Z. Zhang, H. Shang, X. Zhang, C. Liu, S. Li, Z. Wen, S. Ji and J. Sun, *ACS Appl. Energy Mater.*, 2021, **4**, 5113–5122.

32   J. Cao, D. Zhang, X. Zhang, S. Wang, J. Han, Y. Zhao, Y. Huang and J. Qin, *Applied Surface Science*, 2020, **534**, 147630.

33   X. Liu, Y. Li, L. Zeng, X. Li, N. Chen, S. Bai, H. He, Q. Wang and C. Zhang, *Advanced Materials*, 2022, **34**, 2108327.

34   E. Trevisanello, R. Ruess, G. Conforto, F. H. Richter and J. Janek, *Advanced Energy Materials*, 2021, **11**, 2003400.

35   A. Ch. Lazanas and M. I. Prodromidis, *ACS Meas. Sci. Au*, 2023, **3**, 162–193.

36   X. Jin, Z. Zhu, Q. Miao, C. Fang, D. Huang, R. Giovine, L. Chen, C. Dun, J. J. Urban, Y. Fu, D. Li, K. Liu, Y. Wang, T. Zhu, C. Zhu, W. Tong and G. Liu, *Advanced Science*, 2025, **12**, 2416995.

37   W.-G. Lim, X. Li and D. Reed, *Small Methods*, 2024, **8**, 2300965.

38   Y. Dai, J. Zhang, X. Yan, G. Zhao, M. Yang, J. Xiong, R. Li, N. Miao, H. Yu, M. Hu, J. Liu and J. Yang, *Chemical Engineering Journal*, 2023, **471**, 144158.

39   M. H. Alfaruqi, V. Mathew, J. Gim, S. Kim, J. Song, J. P. Baboo, S. H. Choi and J. Kim, *Chem. Mater.*, 2015, **27**, 3609–3620.

40   J. Chacón-Borrero, X. Chang, Z. Min, J. Yu, G. Montaña-Mora, K. V. Mejia-Centeno, Y. Sun, X. Zhou, S. Tunmee, P. Kidkhunthod, J. Li, J. Llorca, J. Arbiol and A. Cabot, *Energy Storage Materials*, 2025, **81**, 104486.

Journal of Materials Chemistry A Accepted Manuscript

Dr. Sanja Tepavcevic
Argonne National Laboratory
9700 S. Cass Avenue, Argonne, IL, USA 60439
Phone +1-630-252-5387
Email: sanja@anl.gov

October 31, 2025.

Dear Editor,

The authors confirm that the data supporting the findings of this study are available within the article [and/or] its supplementary material.
Should any raw data files be needed in another format they are available from the corresponding author upon reasonable request.

Sincerely,

Dr. Sanja Tepavcevic

Journal of Materials Chemistry A Accepted Manuscript